A pencil beam algorithm for proton dose calculations

To cite this article: Linda Hong *et al* 1996 *Phys. Med. Biol.* **41** 1305

View the article online for updates and enhancements.

A pencil beam algorithm for proton dose calculations

Linda Hong†‡, Michael Goitein†, Marta Bucciolini§, Robert Comiskey†,
Bernard Gottschalk∥, Skip Rosenthal†, Chris Serago† and Marcia Urie†

† Department of Radiation Oncology, Massachusetts General Hospital, Boston, MA, USA
‡ Department of Radiation Oncology, Mt Sinai Medical Center, New York, NY, USA
§ Department of Medical Physics, University of Florence, Florence, Italy
∥ Harvard Cyclotron Laboratory, Harvard University, Cambridge, MA, USA

Abstract. The sharp lateral penumbra and the rapid fall-off of dose at the end of range of a proton beam are among the major advantages of proton radiation therapy. These beam characteristics depend on the position and characteristics of upstream beam-modifying devices such as apertures and compensating boluses. The extent of separation, if any, between these beam-modifying devices and the patient is particularly critical in this respect.

We have developed a pencil beam algorithm for proton dose calculations which takes accurate account of the effects of materials upstream of the patient and of the air gap between them and the patient. The model includes a new approach to picking the locations of the pencil beams so as to more accurately model the penumbra and to more effectively account for the multiple-scattering effects of the media around the point of interest. We also present a faster broad-beam version of the algorithm which gives a reasonably accurate penumbra. Predictions of the algorithm and results from experiments performed in a large-field proton beam are presented. In general the algorithm agrees well with the measurements.

1. Introduction

As the number of proton therapy facilities has steadily increased during recent years, the development of accurate algorithms for proton beam dose calculations has become of some interest. Extensive experiments and Monte Carlo simulations performed by various investigators over the years (Urie *et al* 1986a, b, Sisterson *et al* 1989) have provided information as to what effects should be included in a reasonably accurate dose algorithm. As demonstrated by Urie *et al* (1986a, b) and Sisterson *et al* (1989) internal inhomogeneities in the patient and beam-modifying devices upstream of the patient, such as apertures and compensating boluses, significantly affect the proton beam characteristics, such as the sharp lateral penumbra and the rapid fall-off of the dose at the end of range. The extent of the separation, if any, between beam-modifying devices and the patient has been found to be critical in respect of the penumbra-blurring effect.

The dose algorithms used now in routine clinical practice are broad-beam models, based on ray-tracing techniques with the water-equivalent depth to a point of interest in a patient being calculated along the beam direction to that point and the dose associated with that depth being extracted from dose distributions as measured in water phantoms. These broad-beam models do not fully model the dose perturbations induced by complex heterogeneous regions. They also do not take proper account of the penumbra-blurring effect of the beam-modifying devices upstream of the patient. Recently, there have been several accounts of

proton beam dose algorithms (Lee *et al* 1993, Petti 1992, Scheib *et al* 1992). Lee *et al* proposed a broad-beam model which takes into account the penumbra-blurring effect of the patient only. Petti showed that a proton pencil beam algorithm, which models the multiple-Coulomb-scattering effect due to inhomogeneities in the patient, is more accurate but more time consuming than a ray-tracing model. The effect of the position of materials upstream of the patient was not addressed in Petti's work.

In this paper, we present a pencil beam algorithm for proton dose calculations which takes accurate account of the effects of materials upstream of the patient and of the air gap between them and the patient. Similarly to the Gaussian pencil beam model used for electron beams formulated by Hogstrom *et al* (1981), the pencil beam dose distribution is separated into a central-axis term and an off-axis term. The central-axis term of the pencil beam dose distribution is related to the measured broad-beam central-axis depth dose in a water phantom by an effective depth and inverse square correction. The off-axis dependence of the pencil beam dose distribution is described by a Gaussian distribution whose standard deviation is calculated by adding in quadrature the multiple-Coulomb-scattering contributions from each beam-modifying device and from the patient. The model calculates the multiple Coulomb scattering based on the generalized Highland formula as described by Gottschalk *et al* (1993). The algorithm includes a new approach to picking the locations of the pencil beams so as to more accurately model the penumbra and to more effectively account for the multiple-scattering effects of the media around the point of interest. For each point of interest, the contributing pencil beams are sampled in polar coordinates centred at the point of interest. The choice of sampling points is point of interest dependent.

We also present a broad-beam version of the algorithm which estimates dose with a reasonably accurate penumbra and can compute in a much shorter time. The broad-beam algorithm correctly models the variation of penumbra with depth within the patient and with the thickness, composition and location of upstream materials. In particular, the penumbra is affected by the size of any air gap between the bolus and the patient. This faster broad-beam version is useful for initial beam-planning purposes.

The pencil beam algorithm and the broad-beam version are both fully implemented into a treatment planning system. Predictions of the algorithm and results from experiments performed in a large-field proton beam at Harvard Cyclotron Laboratory are presented and discussed.

2. Materials and methods

2.1. Beam line geometry

The beam line geometry modelled in this algorithm is shown in figure 1. This geometry is rather general; furthermore, the algorithm can be trivially adopted to other arrangements of beam line elements. This geometry models the beam lines at the Harvard Cyclotron Laboratory.

Beam-modifying devices are divided into two types: beam-limiting devices and non-beam-limiting devices. The beam-limiting devices are devices, such as collimators, apertures and blocks, which limit the beam laterally. They are considered to be ideal, that is to 'pass' the beam unaltered through their open regions and to block it entirely elsewhere. We do not model the so-called 'slit scattering' of the proton beam by apertures (Mayo *et al* 1993, Gottschalk *et al* 1994). Non-beam-limiting devices affect protons differently. Rather than block them entirely, they cause them to lose energy and to scatter. The loss of energy means that the proton will penetrate less deeply within the patient than if the beam-
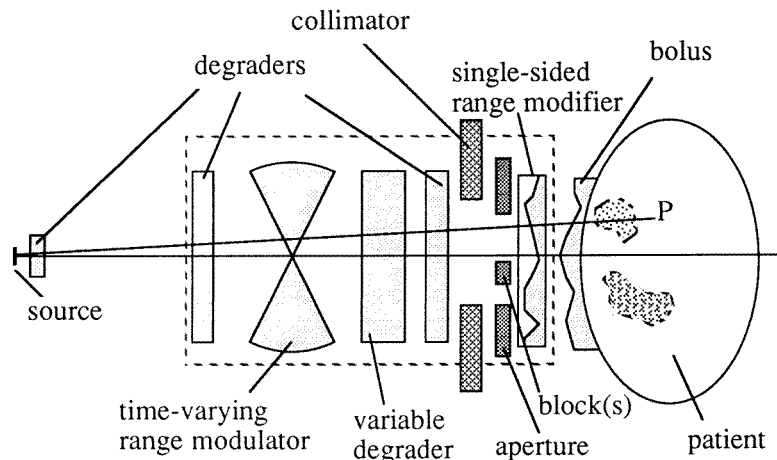
Figure 1. The beam line geometry.

modifying devices were not there. The scattering increases the beam penumbra and may affect the dose within the patient and near the end of range. The non-beam-limiting devices considered in the algorithm are degraders (material of uniform thickness intercepting the entire beam), a range modulator and a range modifier (compensating bolus). The distances of the beam-modifying devices from the source are taken to be the downstream face of the device.

2.2. Input data

We define the 'open beam' as the proton beam free of any beam-modifying devices other than those which are always in the beam, namely, the beam-spreading system, monitoring ion chambers and the collimator support system. The open beam also excludes the range modulator and hence is a so-called pristine (near-monoenergetic) Bragg peak—not a spread-out Bragg peak. In our algorithm, the open beam is modelled as an effective source with a finite effective size, located at an effective point in space. The distance from the effective source to the isocentre is the source–axis distance. The size of the effective source is parametrized by a two-dimensional Gaussian distribution whose standard deviation is the effective radius of the source. The source–axis distance is determined from experiments by measuring the dose output of the open beam in air and assuming it should obey an inverse square law. The effective source size is determined by measuring the penumbra of the open beam in air with a straight-edged block on the beam axis. Our algorithm requires the effective source radius and source–axis distance as input. It also requires as input the central-axis depth dose of the open beam in a water phantom. For different beam-spreading systems, we expect different effective sources and central-axis depth doses.

2.3. Coordinate systems

We primarily use the beam's-eye-view (BEV) coordinate system, with its origin located at the beam's source. The z axis is along the central axis of the beam. The value of the BEV coordinate system is in assessing the geometrical relationships among the various beam-modifying devices which lie along the beam line.

It is common to compute 2D coordinates in a plane perpendicular to the beam at any of several levels (depending on the calculational need). 2D coordinates in a plane through the point of interest are represented as (x_p, y_p). 2D coordinates in the plane through a device (usually its downstream surface) are represented as (x_{dev}, y_{dev}).

2.4. Physical properties modelled

Protons in the energy range of interest for radiation therapy undergo two main processes: energy loss and small-angle scattering. These processes, of course, take place both as protons pass through the various beam-modifying devices, and as they come to rest in the patient.

Protons lose energy primarily through multiple Coulomb interactions. As a population of protons traverse a given absorber their mean energy is reduced and some (relatively modest) spread in energy occurs due to statistical fluctuations. We use measured depth–dose curves to characterize the dose against residual range of protons, rather than use fundamental theory (Janni 1966 and references therein) to compute this relationship. The measured depth–dose curve also takes statistical fluctuations into account since its shape necessarily includes range-straggling effects. We characterize degraders by the mean range loss they cause. (For computational simplicity, and because there is a one-to-one relationship between mean energy and mean penetration (Barkas and Berger 1964), we track the residual range of the protons rather than their energy.) If degraders were of the same composition as the material (water) in which the depth–dose curve is measured then the range reduction of a degrader would just be equal to its thickness. To allow for different compositions of materials, we use a correction factor, as described in the appendix, to convert the degrader thickness to a water-equivalent thickness. (All material thicknesses are specified in terms of the water-equivalent thickness.)

The multiple scattering of protons by the material through which they pass causes angular emittance (angular standard deviation of the distribution) in the beam which ultimately increases the size of the penumbra and affects the way internal and external inhomogeneities perturb the dose. The shape of the angular distribution as the result of the multiple Coulomb scattering is nearly Gaussian for small angles and deviates from Gaussian at larger angles (Gottschalk *et al* 1993). The non-Gaussian tails contain, however, only a small fraction of protons and we therefore ignore them in our algorithm. It would be straightforward to extend the algorithm to include wide-angle scattering effects.

We include, without theoretical rigour, the effects of nuclear interactions through the stratagem of basing our algorithm on a measured depth–dose curve. This, of course, includes the does consequences of nuclear interactions. The influence of these events on the angular emittance of the beam is not taken into account since they are relatively infrequent.

The beam-modifying devices are ordered as they appear along the beam line. The present implementation assumes that the devices are encountered in the following sequence: (i) any degraders upstream of the range modulator (their effect is neither point of interest (POI) nor range modulator dependent); (ii) the range modulator; (iii) any degraders downstream of the range modulator (their effect is not POI dependent, but is range modulator dependent); (iv) the beam-limiting devices (a collimator (always present), an aperture and blocks); (v) the range modifier (either single sided or double sided) and (vi) the patient.

Protons are assumed to emanate axial symmetrically from the finite-sized source with a specified mean residual range (i.e. initially it is a near-monoenergetic beam) and, initially, with no angular emittance. From the point of view of range modification, each device acts in a straightforward manner to reduce the residual range of the protons, as described below.

In terms of the angular emittance induced by the devices, we adopt the following strategy:

(i) scattering in devices upstream of the beam-limiting device(s) is taken as increasing the effective source size;

(ii) scattering in devices downstream of the beam-limiting device(s) is taken as increasing the radial emittance (spatial standard deviation of the distribution) at the depth of the point of interest and

(iii) scattering in the patient is taken as increasing the radial emittance at the depth of the point of interest.

As protons reach each beam-modifying device, its influence on the beam is computed. The following descriptions indicate how each element is modelled.

2.4.1. Degraders. The residual range loss in each degrader, t_{deg}, with units of grams per square centimetre water equivalent, is given by

$$t_{deg} = l_{deg} \, \text{WER}_{deg} \, \rho_{deg} \tag{1}$$

where l_{deg} is the physical thickness in centimetres, ρ_{deg} is the density of the material in grams per cubic centimetre, and WER_{deg} is the water-equivalent ratio of the material as defined in the appendix.

Multiple Coulomb scattering from degraders upstream of the beam-limiting devices will cause angular emittance of the beam. Protons can lose a substantial fraction of their energy in the degraders, but not all of it. The beam line degraders are therefore considered to be of intermediate thickness, and their influence on angular emittance is calculated as described in the appendix. The angular emittance primarily exhibits itself as a broadening of the penumbra, as indicated schematically in figure 2. We therefore represent it as an effective enlargement of the source. The contribution to the source size from the angular emittance of the degrader, σ_{deg}, is given (in the small-angle approximation which we use here) by

$$\sigma_{deg} = \theta_{deg}(z_{deg} - l_{deg} + l'_{deg}) \tag{2}$$

where θ_{deg} is the characteristic scattering angle of the degrader, as computed using equation (A1) of the appendix. For computational speed, θ_{deg} is determined in practice from look-up tables of $\theta_0(t)/\theta_0(R)$ and $\theta_0(R)$ as depicted graphically in figure A2. z_{deg} is the distance from the source to the downstream face of the degrader. l'_{deg} is the distance of the effective origin of scattering of the degrader from its upstream face. That distance is characteristically approximately half the thickness of the degrader. However, we use the more accurate estimation, as described in the appendix, using a look-up table which contains the values shown in figure A3.

If there are degraders downstream of the beam-limiting devices (which is not the case in the beam line we are primarily interested in modelling) they are modelled as contributing to the radial smear within the patient, as described below for single-sided range modifiers. Their contribution to the radial smear is given by

$$\sigma_{deg} = \theta_{deg}(z_p - z_{deg} + l_{deg} - l'_{deg}) \tag{3}$$

where z_p is the distance from the source to the point of interest.

2.4.2. The range modulator. The Bragg peak of near-monoenergetic proton beams is too narrow for most radiation therapy purposes. Dose is spread out in depth by one of a number of stratagems. Here we model the rotating wheel which carries a set of variable-thickness degraders, first described by Wilson (1946) and developed by Koehler *et al* (1975). In
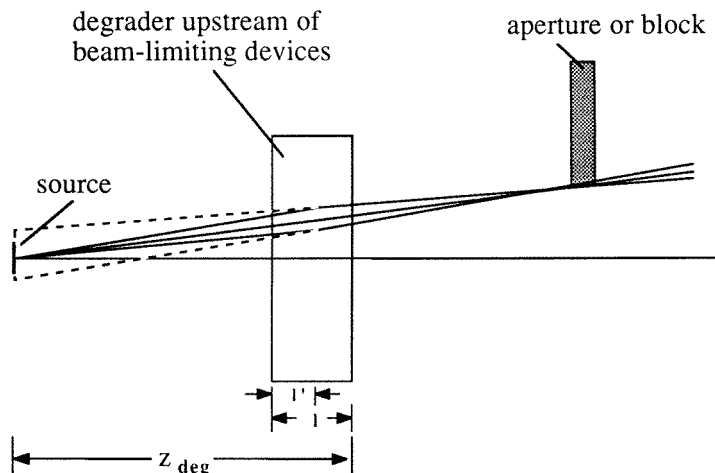
Figure 2. A schematic drawing of the angular emittance caused by multiple Coulomb scattering in a degrader upstream of the beam-limiting device(s). *l* is the physical thickness of the degrader and *l′* identifies the effective scattering origin of the degrader, as discussed in the appendix.

our algorithm, the range modulator is treated as a set of degraders which are included in the beam, one by one, for a given proportion of the time determined by the 'weight factor' assigned to each degrader. The beam modulation, then, initiates a loop over the modulator elements. Since the influence on the beam of any material downstream of the range modulator is affected by the range modulator itself, their range loss and scattering effects have to be considered separately for each modulator element. In all other respects, the range modulator acts like a degrader.

2.4.3. Beam-limiting devices. Beam-limiting devices (collimators, apertures and blocks) are assumed to completely absorb protons which impinge upon them, and to transmit all other protons without affecting them. We thus ignore those particles which scatter out of a beam-limiting device before losing all their energy. Such edge scattering has been shown (Mayo *et al* 1993, Gottschalk *et al* 1994) to introduce a low-energy contamination into the beam which can significantly affect the dose at smaller depths.

2.4.4. The range modifier. Range modifiers—also described as compensating boluses— are, in effect, degraders whose thickness varies throughout the field cross-section. Such devices are used to control the beam penetration to (i) tailor the distal beam penetration to the desired depths, (ii) compensate for internal inhomogeneities and (iii) compensate for curvature of the entrance surface (Urie *et al* 1984). Two types of range modifier are supported: a single-sided range modifier and a double-sided range modifier or bolus, as it is often termed, which is in contact with the patient's external surface. Range modifiers are treated separately from degraders because their thickness is not uniform but, rather, depends on the point of interest whose dose is being calculated.

The range loss, $t_{rm}(x_{rm}, y_{rm})$, due to the thickness of the range modifier material at the position (x_{rm}, y_{rm}) within the range modifier is given by

$$t_{rm}(x_{rm}, y_{rm}) = l_{rm}(x_{rm}, y_{rm}) \, \mathrm{WER}_{rm} \, \rho_{rm} \tag{4}$$
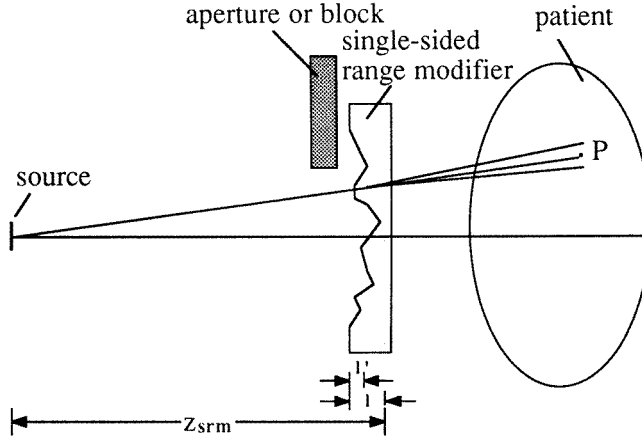
Figure 3. A schematic drawing of the radial emittance caused by multiple Coulomb scattering in a single-sided range modifier. l and l' are respectively the physical thickness and the effective scattering origin of the range modifier for the point of interest.

where $l_{rm}(x_{rm}, y_{rm})$ is the physical thickness in centimetres at (x_{rm}, y_{rm}), ρ_{rm} is the density of the material in grams per cubic centimetre and WER_{rm} is the water-equivalent ratio of the material as defined in the appendix.

Since the range modifier is downstream of the beam-limiting devices, we represent the scattering effect by the radial emittance it causes at the depth of the point of interest, as suggested in figure 3. The approach to scattering taken in our algorithm depends on whether the range modifier is single or double sided.

The radial emittance from a single-sided range modifier is schematically shown in figure 3. The effective origin of scattering of the range modifier, l'_{srm}, and the scattering angle θ_{srm} are obtained from look-up tables of the values in figures A2 and A3. The radial emittance at the depth of the point of interest is given by

$$\sigma_{srm} = \theta_{srm}(z_p - z_{srm} + l_{srm} - l'_{srm}) \tag{5}$$

where z_p is the distance from the source to the point of interest and z_{srm} is the distance from the source to the downstream face of the range modifier. Note that the drift space contribution in the above equation naturally includes any air gap between the range modifier and the patient.

Double-sided range modifiers are taken into account as simply adding to the size of the patient, and treated as described below. The amount added to the radiographic path length is equal to the thickness of the range modifier, t_{rm}, given in grams per square centimetre water equivalent. This assumes that the scattering power of the bolus is similar to that of tissue, an assumption that is reasonable in the case of the materials we are contemplating using for double-sided boluses.

2.4.5. The patient. The patient is different from all other elements because one generally wishes to know the dose at arbitrarily chosen points within him or her. As a consequence, protons may continue past, stop at or near or never reach the point of interest. The dose at a point of interest is determined, then by the residual range of protons directed at and, in the case of the pencil beam algorithm, near to that point. This is equal to the residual range

of protons entering the patient, minus the radiographic path length from the surface to the point of interest, $p(x_p, y_p, z_p)$. The radiographic path length from the surface to the point of interest, rpl_p, is based on a pixel-by-pixel integration through a CT study, given by

$$\text{rpl}_p = \int_{surface}^{z_p} dz' \, \text{WED}(\text{CT}(z')) \tag{6}$$

where $\text{CT}(z')$ is the CT value at the point a distance z' along the path of integration, and WED is value from a look-up table which converts between CT value and water-equivalent density, as has been described by Chen *et al* (1979).

The calculation of the contribution to radial emittance by the patient is somewhat different from that for a single-sided range modifier, since the patient constitutes an infinitely thick degrader as described in the appendix, and now the point of interest is inside the 'degrader'. The theory of radial emittance in an infinitely thick degrader is referenced in the appendix; look-up tables corresponding to the values shown in figure A4 are used to obtain the radial emittance from the patient (including the double-sided range modifier, if any), σ_{pt}:

$$\sigma_{pt} = y_0(\text{rpl}_p) \tag{7}$$

where y_0 is as described in the appendix.

2.4.6. The summation of the effects of all beam line elements. The effect of devices and of the patient on the proton residual range (i.e. energy) is accumulated in a linear subtractive manner. At the source, each proton is assigned an initial residual range; that value is reduced as each device is encountered. (Any energy spread in the protons is accounted for through the use of a measured depth–dose curve.) The residual range at the depth of the point of interest is used to look up the central axis dose from the measured open beam depth–dose distribution.

So far as scattering effects are concerned, as described above, when protons reach the point of interest, the total Gaussian radial emittance (standard deviation) is composed of three components: (i) the radial emittance due to the effective source size, σ_{size}, which itself is composed of the physical source size of the open beam plus any contributions added in quadrature from the angular emittance due to scattering in each degrader upstream of the beam-limiting devices; (ii) the radial emittance due to scattering of the single-sided range modifier, σ_{srm}, if any, and (iii) the radial emittance due to multiple scattering within the patient (plus the double-sided range modifier, if any), σ_{pt}. The contributions from these three components are added in quadrature to provide the total standard deviation of the radial distribution of the pencil beam profile, σ_{tot}, assumed to be Gaussian, at the depth of the point of interest:

$$\sigma_{tot} = \left[\sigma_{size}^2 \left(\frac{z_p - z_{bld}}{z_{bld}} \right)^2 + \sigma_{srm}^2 + \sigma_{pt}^2 \right]^{1/2} \tag{8}$$

where z_{bld} is the distance from the source to the downstream face of the beam-limiting device. When more than one beam-limiting device is in the beam, we use the location of that which most nearly limits the beam for the point of interest.

2.5. The pencil beam algorithm

The pencil beam algorithm approximates the full beam by a set of elemental pencil beams. The dose at any point is taken to be the sum of the doses delivered by each of the pencil

beams. The algorithm is composed then of two parts: the computation of the dose at a point of interest from a given pencil beam; and the technique for summing the contributions of the pencil beams.

(i) *Dose contribution of a single pencil beam.* To compute the dose at a point of interest from a given pencil beam, we follow the approach of Hogstrom *et al* (1981) who reported on a pencil beam algorithm to model electron beams. The dose, $d(x', y', z')$, at the point (x', y', z') due to a pencil beam is separated into a central-axis term, $C(z')$, and an off-axis term, $O(x', y', z')$:

$$d(x', y', z') = C(z')O(x', y', z').$$ (9)

Here, the coordinates are taken to be in the frame which has its origin at the source and its z' axis along the axis of the pencil beam.

The central-axis term is simply taken from the measured broad-beam central-axis depth dose in a water phantom—modified by an inverse square correction:

$$C(z') = \text{DD}(d_{eff}) \left(\frac{\text{ssd}_0 + d_{eff}}{z'} \right)^2$$ (10)

where DD is the central-axis depth–dose distribution of the open beam in a water phantom and ssd_0 is the source-to-surface distance when the open beam depth–dose data was measured. d_{eff} is the effective depth given by

$$d_{eff} = R_0 - (R_r - \text{rpl}(z'))$$ (11)

where $\text{rpl}(z')$ is the radiographic path length along the pencil axis to the depth of the point (x', y', z'), R_0 is the initial residual range and R_r is the residual range as the protons enter the patient.

The off-axis term, $O(x', y', z')$, is taken to be the lateral flux distribution from the radial emittance suffered by protons directed along the axis of the pencil beam. The distribution is taken to be Gaussian:

$$O(x', y', z') = \frac{1}{2\pi[\sigma_{tot}(z')]^2} \exp\left(-\frac{x'^2 + y'^2}{2[\sigma_{tot}(z')]^2} \right)$$ (12)

where $\sigma_{tot}(z')$ is the radial emittance standard deviation calculated by adding in quadrature the contributions from the source, from every beam modifying device and from the patient, as discussed above. The normalization is such that integrating the dose over an infinite area of equally weighted pencil beams, i.e. modelling an open beam, gives back the open beam depth–dose distribution.

(ii) *Integrating the effect of all pencil beams.* The dose distribution of a practical beam is determined by integration over all pencil beams which may contribute to it. This expression makes the approximation that the off-axis distance of the point of interest relative to a pencil beam may be taken in the plane perpendicular to the beam's central axis (which is slightly slanted relative to the pencil's central axis). In the coordinate frame with the origin at the source and the z axis along the central axis of the incident beam, the dose for the point of interest at (x, y, z) is then given by

$$D(x, y, z) = \int \int \text{d}x' \text{d}y' \Psi_0(x', y') \frac{C(x', y', z)}{2\pi[\sigma_{tot}(x', y', z)]^2} \exp\left(-\frac{(x'-x)^2 + (y'-y)^2}{2[\sigma_{tot}(x', y', z)]^2} \right)$$ (13)

where $\Psi_0(x, y)$ is the intensity profile of the open beam and the integration is over the beam area (and need not be extended outside the most extreme beam-limiting device since $\Psi_0(x, y)$

is then everywhere zero). $C(x', y', z)$ is the central-axis term of the dose distribution of the pencil beam located at (x', y'), including an inverse square correction.

In practice, to evaluate the integration of the pencil beam distributions, we convert the integration into a summation of pencil beams.

2.5.1. Adaptive sampling of pencil beams in polar coordinates. In summing the pencil beams, one must determine how to sample them. The traditional way is to sum over pencils which form a rectilinear grid where they intersect a plane normal to the central axis of the beam. When the dose needs to be sampled at each of many points of interest, it is more efficient to sum over all pencils which contribute to the beam, and accumulate the dose at each sampling point for each pencil beam. However, we have generally favoured approaches to dose analysis which use a lesser number of computed points. For that reason, and to more accurately calculate dose in the region of the penumbra, the outer loop of our algorithm is over the points of interest, and for each point we sum the effects of a number of pencil beams.

We choose pencils on a *polar coordinate grid*. We have used a novel adaptive approach to the choice of grid pattern and size for the pencil beams. In setting the azimuthal spacing we divide the circle into n_θ equal sectors. The number of samples taken is, of course a matter of balancing accuracy against computational speed. Typically we use $n_\theta = 12$—i.e. sample along spokes at $30°$ intervals. *The radial spacing is adaptive*—that is, it depends on the point of interest. It depends on the radial emittance which is obtained at or near the calculation point, and it is tailored to the beam-limiting device(s) in order to model the penumbra as accurately as possible. In addition, the algorithm sums *finite-sized pencils*, integrated over sectors in polar coordinate space, rather than infinitely thin pencils. The polar grid is set up as follows.

For every point of interest (POI) for which the dose is to be calculated, we set up a polar grid in a plane perpendicular to the central axis of the incident beam, so effectively the polar grid is sampled in a plane perpendicular to the central axis of the incident beam. The radial spacing of the grid depends on the scattering of the protons at or near the POI. Since protons will generally be scattered more as they penetrate deeper inside the patient, the radial spacing is enlarged the deeper the POI is inside the patient, according to the following scheme.

For each POI, we calculate the total radial emittance (standard deviation) of the pencil beam from the source to the POI, $\sigma_p^{phantom}$, assuming that the range modifier thickness is set equal to its thickest value (to avoid a too small pencil grid coverage for POIs at the surface of the patient when the range modifier shadowing the POI is very thin) and that the material between the patient surface and the POI is water equivalent. Then we set the maximum sampling radius, r_{max} as follows:

$$r_{max} = 3\sigma_p^{phantom}. \tag{14}$$

Contributions from larger radii are considered negligible. For each $360/n_\theta°$ sector we then choose n_r radial boundaries for the (finite-sized) pencil beams: typically we use $n_r = 10$. We choose the radial boundaries at intervals of r_{max}/n_r—provided that none of the resulting pencil beams are intersected by the contours of any beam-limiting devices. If this is not the case we proceed as follows. We find all the intersections of the spoke with the beam-limiting devices, using the method of Siddon (1985). For each spoke section spanning the open field, we divide the spoke section into the smallest number of pencil beams which have a radial size of no more than r_{max}/n_r. Pencil beams which abut a beam-limiting device edge will be given a 50% weight when summing their dose contributions.
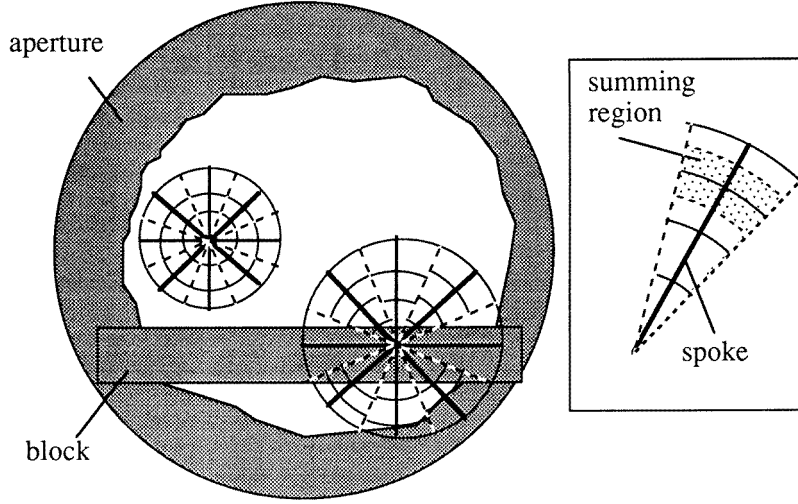
Figure 4. Two pencil beam sets as seen in the BEV.

Figure 4 shows a BEV of two sampling grids for two POIs: one in an open field region (with $n_\theta = 8$ and $n_r = 3$ for clarity); the other near two beam-limiting devices.

In this adaptive radial spacing scheme, $\sigma_p^{phantom}$ is used as a spatial scale for pencil beam samples for each point of interest. For the large-field beam with a contoured scattering system at HCL, if the beam has a 11.8 cm range modulator wheel and a uniform 3.55 g cm^{-2} water-equivalent preabsorber with 6 cm air gap between the aperture and water tank, $\sigma_p^{phantom}$ is about 1.6 mm at 1.2 cm depth. For the same beam configuration, $\sigma_p^{phantom}$ is about 3.6 mm at 10.2 cm depth.

2.5.2. Dose summation. In summing the contributions of individual pencils, we integrate over the area of the summation regions defined on the polar grid described above, as shown in the inset of figure 4. Consequently, we describe each pencil in the summation as being of finite area evaluated as follows:

$$
\begin{aligned}
F_p^{i,n} &= f_n \frac{\delta\theta}{2\pi(\sigma_p^{i,n})^2} \int_{r_n'}^{r_n''} \mathrm{d}r\, r \exp\left(-\frac{r^2}{2(\sigma_p^{i,n})^2}\right) \\
&= f_n \frac{\delta\theta}{2\pi} \left[\exp\left(-\frac{r_n'^2}{2(\sigma_p^{i,n})^2}\right) - \exp\left(-\frac{r_n''^2}{2(\sigma_p^{i,n})^2}\right)\right]
\end{aligned}
\tag{15}
$$

where $\delta\theta \ (= 360°/n_\theta)$ is the angular increment of the pencil wheel and $\sigma_p^{i,n}$ is the standard deviation of the Gaussian distribution of the nth pencil beam for the ith modulator element at the same depth as the POI. r_n' and r_n'' are the radii of the boundary arcs of the subsection occupied by the nth pencil beam. f_n is the area weight of the nth pencil beam. If the pencil beam is at the intersection with the beam-limiting device, the area weight is 0.5. Otherwise, the area weight is 1. The exponential function is tabulated for computation speed.

We can then compute the dose, D_p, for a given POI, as follows:

$$
D_p = A_p \sum_{i=1}^{N_{mod}} w_i \left[\sum_{n=1}^{N_{pb}} \Psi_0^n \mathrm{DD}(d_{eff}^{i,n}) \left(\frac{\mathrm{ssd}_0 + d_{eff}^{i,n}}{z_p}\right)^2 F_p^{i,n}\right]
\tag{16}
$$

where the outer sum is over the range modulator elements, w_i is the weight of the ith modulator element, N_{mod} is the number of range modulator elements, N_{pb} is the number of pencil beams for this POI, $d_{eff}^{i,n}$ is the effective depth of the nth pencil beam for the ith modulator element at the depth of the POI in the patient and $F_p^{i,n}$ is the finite-area summation of the nth pencil beam for the ith modulator element, given by equation (15) above.

A_p is a normalization factor accounting for 'missed' protons which come from outside the finite-sized polar grid,

$$A_p = \left[1 - \exp\left(-\frac{r_{max}^2\,(1 + 1/2n_r)^2}{2(\sigma_p^{phantom})^2}\right)\right]^{-1}.$$ (17)

For $r_{max} = 3\sigma_p^{phantom}$, $n_r = 10$, $A_p = 1.007$.

2.6. The broad-beam algorithm

The pencil beam algorithm, described above, has many advantages of accuracy. However, due to the need to sum over many pencils, it is relatively slow. We have therefore developed a broad-beam version of the algorithm which preserves many of the features of the pencil beam approach, such as taking into account the scattering and range-reducing effects of upstream materials but which is significantly faster.

In this broad-beam algorithm, the dose at any point is determined by the product of a depth–dose term, which is a function of the path length along a ray between the effective source and the point of interest, and an off-axis ratio. The dose, D_p, for a given point of interest, can be computed by analogy with equation (16), as

$$D_p = \Psi_0(x, y) \sum_{i=1}^{N_{mod}} w_i \text{DD}(d_{eff}^i) \left(\frac{\text{ssd}_0 + d_{eff}^i}{z_p}\right)^2 \text{OAR}^i.$$ (18)

Here, $\Psi_0(x, y)$ is the intensity profile of the open beam, d_{eff}^i is the effective depth for the POI over the ith range modulator element, w_i is the weight of the ith modulator element and OAR^i is the off-axis ratio for the POI over the ith modulator element.

The depth–dose term, $C(z)$, is precisely the same as used in the pencil beam algorithm, as defined in equation (10) above.

In computing the OAR, the effect on the penumbra of any beam-limiting device is determined by the distance of closest approach, ε, of the ray joining the source to the POI to the edge of the beam-limiting device, as schematically shown in figure 5. (However, see below for the case where there are multiple beam-limiting devices.)

The projected distance to edge (pde) is simply given by

$$\text{pde} = \varepsilon \frac{z_p}{z_{bld}}.$$ (19)

pde is defined to be positive in the open region of the beam-limiting device, and negative in the blocked region of the beam-limiting device.

The penumbra transmission factor (PTF_k), which characterizes the effect of the kth beam-limiting device on a broad beam due to scattering alone at a distance pde_k from an infinite straight edge, is given by

$$\text{PTF}_k = \frac{1}{2} + \frac{1}{2}\, \text{erf}\left(\frac{\text{pde}_k}{\sqrt{2}\sigma_{tot}}\right)$$ (20)
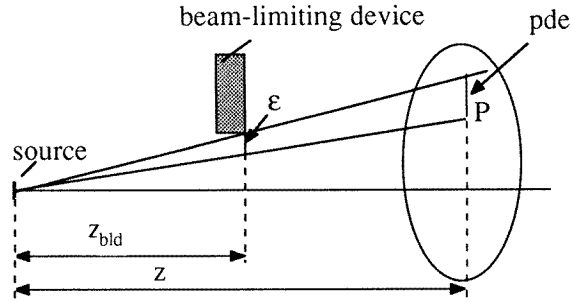
Figure 5. A schematic drawing of the projected distance from a ray between the source and the POI to the edge of a beam-limiting device (pde).
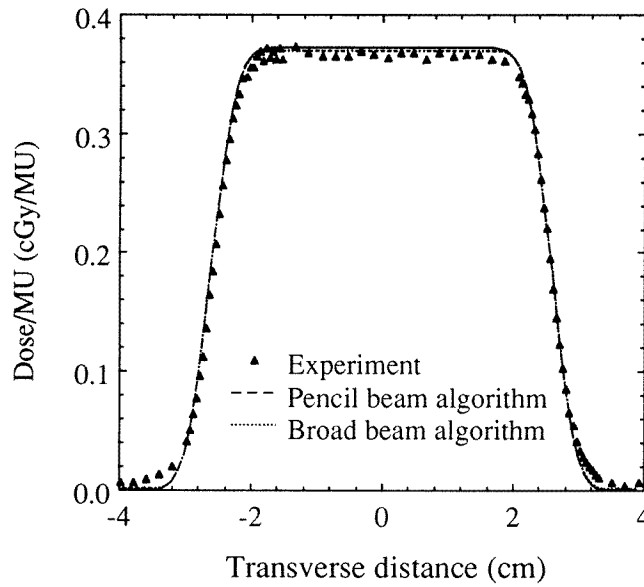

Figure 6. Transverse dose profiles at 6.2 cm depth in water. A uniform single-sided range modifier of 5 g cm^{-2} water-equivalent thickness of Lucite is interposed in the proton beam. The air gap between the range modifier and the front surface of the water tank is 6 cm.

where erf is the standard error function and σ_{tot} is the total standard deviation of the Gaussian distribution profile of the pencil beam from the source to the point of interest. In the program we use a look-up table of values of the error function.

If there is only one beam-limiting device, the off-axis ratio is simply given by

$$OAR = PTF_1. \tag{21}$$

If there is more than one beam-limiting device, we provide two different approaches to approximate their effects.

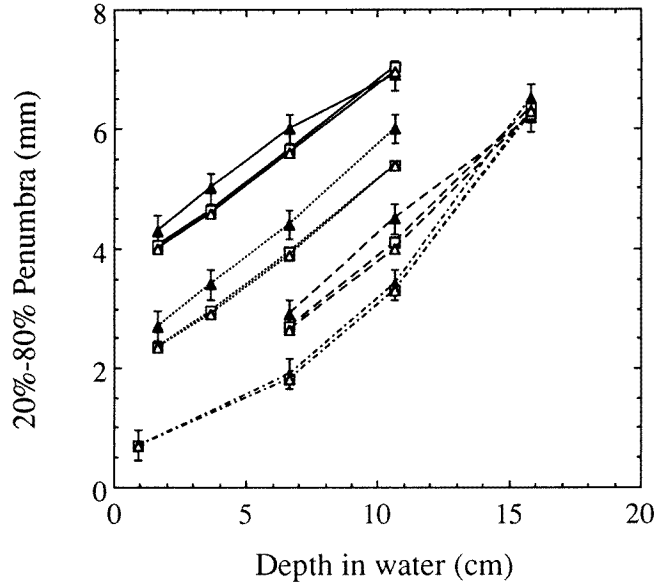(i) *Multiplicative penumbras.* In this mode the penumbra transmission factors of each

Figure 7. Penumbra (80–20% distance) against depth in water for various beam line configurations: solid line, the beam has an 11.8 cm range modulator wheel and a uniform 5 g cm^{-2} water-equivalent Lucite single-sided range modifier; dotted line, the beam has an 11.8 cm range modulator wheel, and a uniform 3.55 g cm^{-2} water-equivalent preabsorber; dashed line, the beam has an 11.8 cm range modulator wheel and no range modifier; dash–dotted line, open beam. Solid triangles are from experimental data, open squares from pencil beam algorithm data and open triangles from broad-beam algorithm data.

beam-limiting device are multiplied together.

$$\text{OAR} = \prod_{k=1}^{N_{bld}} \text{PTF}_k \tag{22}$$

where N_{bld} is the number of beam-limiting devices.

This approach has the advantageous consequence that, where two devices combine to reduce the field area, as in the BEV figure 4 the algorithm will tend to account for the dose-reducing effects of both beam-limiting devices. There is, however, a deleterious consequence: the algorithm will over-sharpen the penumbra if two beam-limiting devices overlie or are close to one another. An example of such a situation is where the aperture and collimator edges too closely approximate one another. One 'solution' in this example is to open up the collimator.

(ii) *The closest-edge mode.* In this mode the smallest of all the penumbra transmission factors is used.

$$\text{OAR} = \min\{\text{PTF}_k\}. \tag{23}$$

This avoids the over-sharpening effect of the multiplicative approach, but underestimates the dose deficit in situations where two devices combine to reduce the field area such as suggested by figure 4.

Of the two modes, we favour the multiplicative one, and reserve the closest-edge mode for investigating unusual edge overlaps.

3. Results

The algorithm has been fully implemented into the 3D treatment planning system, V-TREAT—short for 'Virtual Therapy'—which is being developed at Massachusetts General Hospital. The results presented here are for the particular geometries and beam-line elements of the large-field 160 MeV proton beams at the Harvard Cyclotron Laboratory.

Measurements were made with an automated combined phantom–detection system (Wagner 1992). The open beam depth dose was measured using an Exradin T1 0.05 cm^3 ionization chamber. The cross field profile scans were measured using silicon diodes oriented with their gap in line with the field edge.

Experiments were first conducted to determine the effective source size and the effective source position. These two quantities as well as the depth–dose distribution of the open beam are input to the algorithm. For the large-field beam with a contoured scattering system at HCL, the effective source size was determined to be 2.4 ± 0.1 cm in radius and the effective source-to-isocentre distance was determined to be 537 ± 12 cm. The proton beam fluence was taken to be uniform over the useful beam area.

3.1. The penumbra

We measured the beam penumbra for a number of different beam configurations. Figure 6 shows typical cross-beam profiles at a depth of 6.2 cm. Dashed lines show the predictions of both the pencil beam and the broad-beam algorithms and the measured data are shown as points. Figure 7 shows both calculated and measured penumbra widths (20–80%) at different depths in a water tank for beams with different combinations of beam-modifying devices. Figure 8 shows both calculated and measured penumbra widths (20–80%) at a depth of 6.2 cm in a water tank for a beam with an 11.8 range modulator wheel and a 5 g cm^{-2} water-equivalent single-sided range modifier, with a range of air gaps between the single-sided range modifier and the water tank from 6 to 18 cm. The penumbra predictions of both the pencil beam and broad-beam algorithms on the effects of separation between patient and beam-modifying devices are in good agreement (within ± 1 mm) with measurements. This is particularly satisfying with regard to predictions of the effect on the penumbra of an air gap, since this is a large effect which can have significant clinical implications.

3.2. The depth dose

For a homogeneous phantom, the broad-beam model gives very similar results to the pencil beam model, except for small beams. Figure 9 shows the central-axis depth dose of a large (5×5.6 cm^2) proton beam with an 11.8 cm range modulator wheel. Both algorithms predict the depth dose quite well.

As the aperture size decreases, the depth–dose distribution of a proton beam deviates significantly from the broad-beam Bragg curve due to the multiple-Coulomb-scattering effect (Preston and Koehler 1968). The broad-beam algorithm does not model this effect well. Figure 10(a) shows the predictions of the pencil beam algorithm of the central-axis depth–dose distribution for proton beams with varying circular apertures with radii from 2 cm down to 1 mm. Figure 10(b) shows the corresponding predictions from the broad-beam algorithm. Figure 11 shows a comparison of the predictions of the pencil beam algorithm with measurements for a proton beam with a circular aperture of 2.4 mm radius, and with air gaps between the aperture and the water tank of both 1 and 6 cm. The peak in this case is only about one fifth the height of the broad-beam Bragg peak. The pencil beam
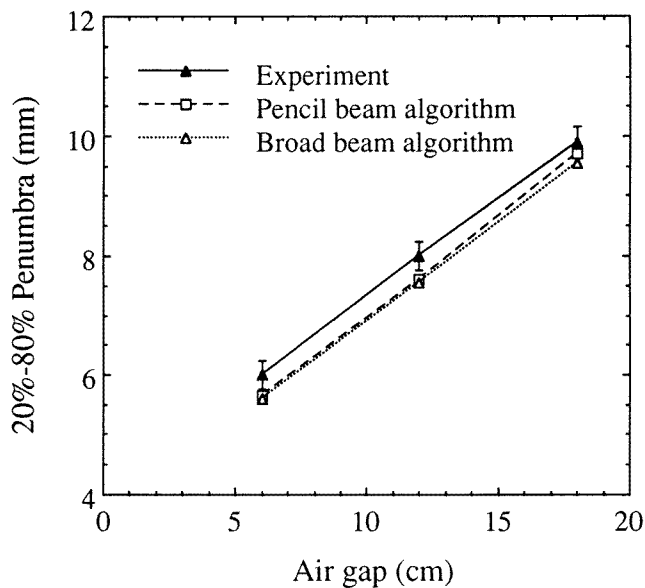
Figure 8. Penumbra (80–20% distance) against air gap. The beam has an 11.8 cm range modulator wheel and a uniform 5 g cm^{-2} water-equivalent Lucite single-sided range modifier.
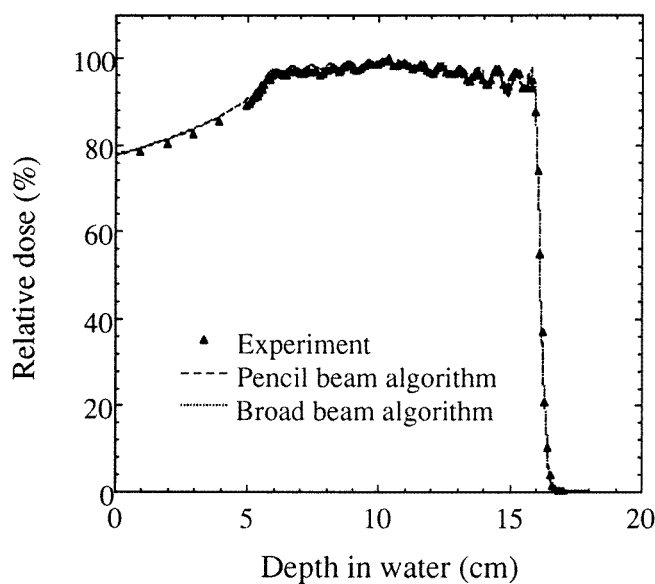

Figure 9. The central-axis depth–dose distribution in a water tank of a proton beam with an 11.8 cm range modulator wheel.

algorithm agrees well with the experimental measurements except in the entrance region. The discrepancy at the entrance region for the 1 cm air gap case is almost certainly due to the 'slit scattering' of protons by the aperture edges (Mayo *et al* 1993, Gottschalk *et al*

Figure 10. Central-axis depth–dose distributions for proton beams of various circular cross-sections as calculated using (a) the pencil beam algorithm and (b) the broad-beam algorithm. Aperture sizes are indicated by their radii.

1994), which is not modelled in our algorithm.

The multiple-Coulomb-scattering effect on small proton beams clearly shows that there are practical limits on how small an aperture can be made (Preston and Koehler 1968). Since the depth–dose characteristics change significantly with proton beam area, a fixed modulator wheel designed for large proton beams may be problematic if used for a small proton beam.

3.3. Inhomogeneities

Any proton dose algorithm must deal both with inhomogeneities which are internal to the patient and with external inhomogeneities. The most important example of the latter is the compensating bolus range modifier which may be interposed in the beam upstream of the patient, generally to compensate for any internal inhomogeneities.
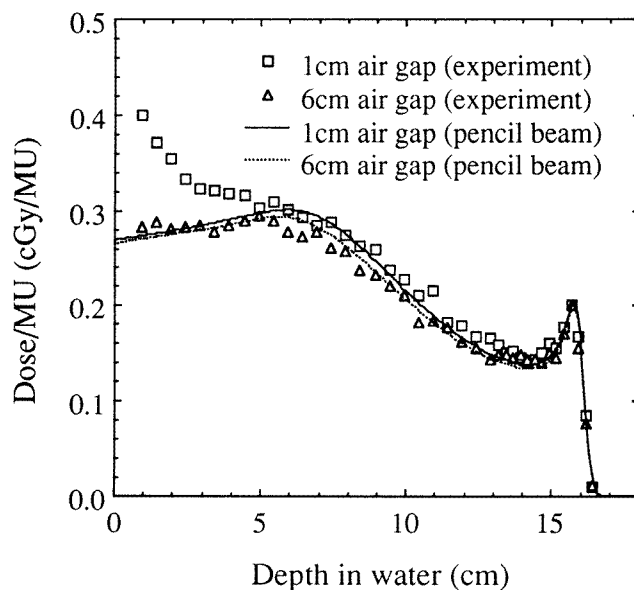
Figure 11. Central-axis depth–dose distributions for the pencil beam algorithm compared with measurements using a diode. The beam is collimated by a 2.4 mm radius aperture. The air gap between the aperture and the water tank is 1 or 6 cm.
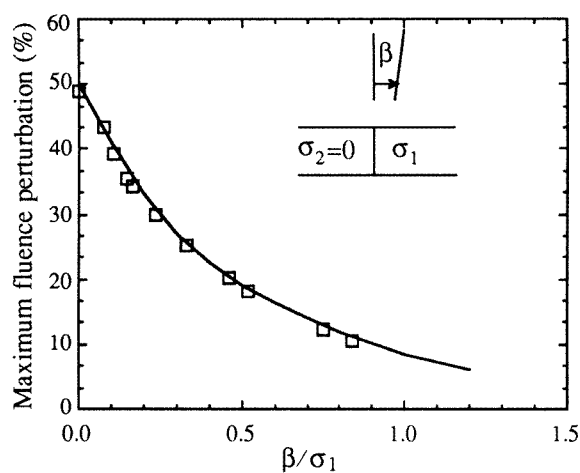

Figure 12. Theoretical and pencil beam algorithm calculations of the maximum fluence perturbation beneath a simple Lucite–air edge exposed to a beam with rms divergence β expressed as a function of β/σ_1. The thickness of the Lucite is 2.5 g cm^{-2} water equivalent.

We compared the predictions from the pencil beam algorithm against the theoretical calculations for thin inhomogeneities (Goitein 1978). Figure 12 shows the results for the maximum fluence perturbation beneath a simple Lucite–air edge, with the thickness of the Lucite at 2.5 g cm^{-2} water equivalent. The agreement is excellent within the computational accuracy.
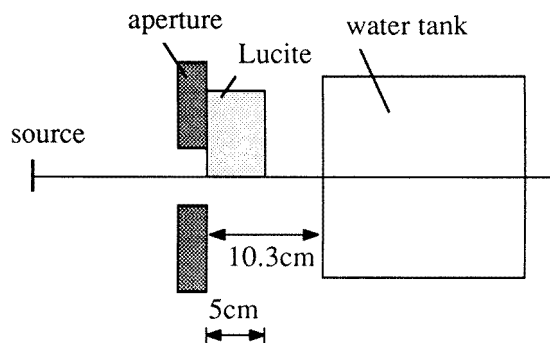
Figure 13. A schematic drawing of the beam line configuration for an external inhomogeneity.

To test the pencil beam algorithm's prediction for Lucite–air inhomogeneities introduced by a range modifier, we investigated the effect of a 5 cm thick Lucite block covering half of the opening of a 5 cm × 5.6 cm aperture, as schematically shown in figure 13. We performed cross-field transverse scans at different depths. Figure 14(a) shows the profile at 0.9 cm depth. The algorithm clearly predicts the cold and hot spots, but there are some discrepancies between the algorithm's predictions and the measured data which are not quantitatively understood. One possible reason is the fact that the effects of nuclear interactions are not included in our algorithm. Nuclear interactions produce low-energy protons in the Lucite, and these protons are scattered into the unblocked side.

The discrepancy is less at larger depths, as can be seen in figure 14(b) which shows the transverse profile at 2.4 cm depth. Figure 14(c) shows profiles at depths near the Bragg peak region on the side covered by the Lucite. In this region, the dose profiles are very sensitive to the depth. As can be seen, the dose profiles predicted by the pencil beam algorithm change dramatically from a 10.37 cm depth to a 10.47 cm depth. Considering the possible experimental positioning error of the scanning diode, which we consider to be approximately ±0.5 mm, we judge that the algorithm gives reasonable results for this region. Figure 14(d) shows the profile at a depth beyond the proton range on the side covered by Lucite. The hump in the measured data is due to the 'slit scattering' of protons from the thick edge of the Lucite, which is similar to the 'slit scattering' effect of protons from apertures (Mayo *et al* 1993, Gottschalk *et al* 1994). The pencil beam algorithm does not model this effect. We have to point out here that a 5 cm thick Lucite–air interface is a worst-case scenario for the pencil beam algorithm. The algorithm gives much better predictions for the thinner Lucite–air interfaces which are encountered in clinical practice.

As far as the effects of the inhomogeneities from the patient are concerned, we expect our pencil beam algorithm will give results similar to those obtained for the pencil beam algorithm of Petti (1992) since the two physical models are essentially the same.

4. Discussion

We have presented a pencil beam algorithm for proton dose calculations which takes into accurate account the multiple-Coulomb-scattering effects of the beam-modifying devices upstream of the patient. We have also presented a faster broad-beam version of the algorithm which gives a reasonably accurate penumbra. The effect on the penumbra of the possible separation between patient and beam-modifying devices, especially the effect of any air gap between the compensating bolus and the patient, are well predicted by both our algorithms.
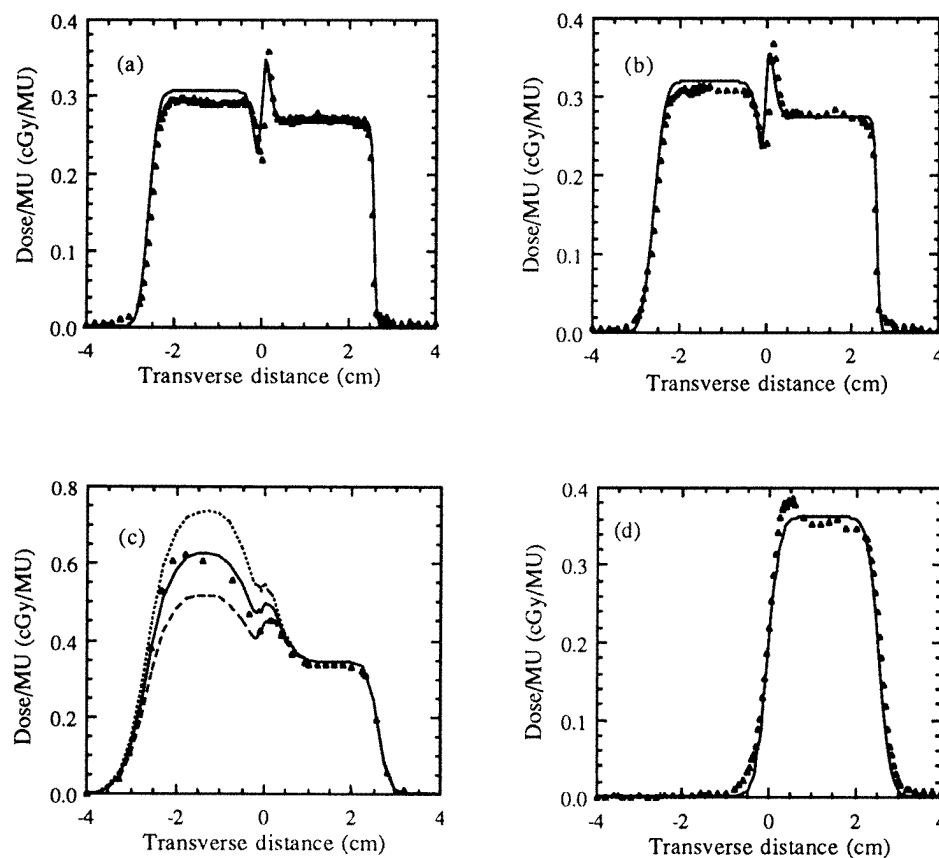
Figure 14. Transverse dose profiles comparing the pencil beam algorithm (solid lines) and measurements (solid triangles) using a diode at a variety of depths in water: (a) 0.9 cm depth in water; (b) 2.4 cm depth in water; (c) 10.42 cm depth in water; dotted line, pencil beam algorithm calculation at 10.37 cm depth in water; dashed line, pencil beam algorithm calculation at 10.47 cm depth in water; (d) 11.4 cm depth in water.

Although, generally speaking, the pencil beam algorithm is more time consuming than the broad-beam algorithm, our approach, based on a separate sampling of pencils for each calculation point, makes it easy (and fast) to calculate only a small number of points. Consequently, a planner can restrict attention to a small region of interest and obtain rapid results using the more accurate pencil beam algorithm. The other advantage of our polar sampling scheme for pencils is its ability to more accurately model the effects of beam-limiting apertures and blocks. It is common that a planner needs to design an aperture with a small protuberance to cover some critical structure. Our approach enables one to account for the protuberance accurately, without having to use a very fine grid.

The computation times are clinically practical. For a beam with a 6 cm diameter aperture, an 11.8 cm modulation depth (with 14 paddles in the wheel), a 3 g cm^{-2} water-equivalent thick Lucite preabsorber and a 3 g cm^{-2} water-equivalent thick Lucite range modifier, the dose calculation for a calculation box size of 10 cm × 10 cm and grid spacing 2 mm (i.e. 2500 points) is about 5 s CPU time for the broad-beam algorithm and 365 s CPU time for the pencil beam algorithm (with $n_\theta = 12$, $n_r = 10$) on a DEC 5000/240 workstation.

There are some limitations of these algorithms which will be the focus of future work. The algorithms do not model the 'slit scattering' from the aperture and collimator. This effect could be substantial at the surface of the patient in some cases (Mayo *et al* 1993, Gottschalk *et al* 1994). The pencil beam algorithm also produces errors in the shadow of thick inhomogeneities whose edge is parallel to the beam's central axis, just as do pencil beam algorithms for electron beams (Hogstrom *et al* 1981). It is likely that Monte Carlo modelling will be the best approach to take to achieve a substantially more accurate modelling of these and other effects.

5. Conclusions

A reasonably accurate and clinically practical proton pencil beam algorithm has been developed. The algorithm takes accurate account of the multiple-Coulomb-scattering effects of the beam-modifying devices upstream of the patient. It predicts accurately the effect on penumbra of beam-modifying devices upstream of the patient and predicts well the effects of external inhomogeneities. A faster broad-beam model has also been developed which allows for faster calculations. The broad-beam model predicts well the penumbra behaviour of the proton beam.

Acknowledgments

Appendix

In this appendix, we summarize the theory of multiple Coulomb scattering of protons as used in the algorithms reported here. Our treatment follows closely that described by Gottschalk *et al* (1993) which should be consulted for details of the calculations.
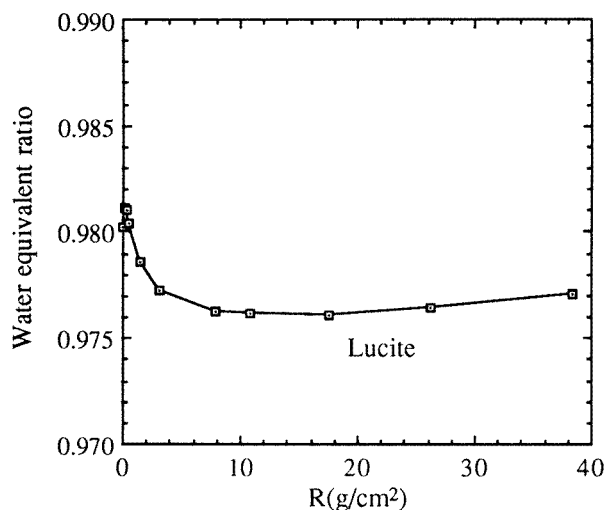

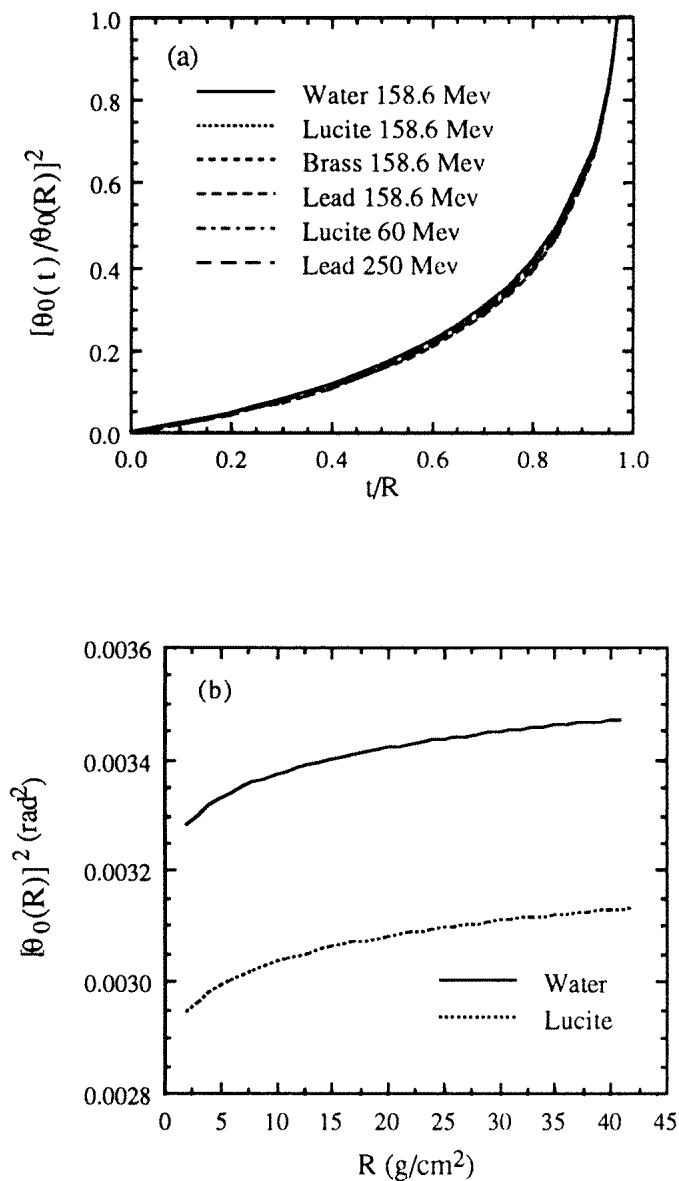**Figure A1.** The WER of Lucite against the mean proton range *R*.

Figure A2. Multiple Coulomb scattering of protons in scatterers of arbitrary thickness with different incident energies. (a) $[\theta_0(t)/\theta_0(R)]^2$ against t/R where t is the areal thickness of the material in grams per square centimetre and R is the mean proton range in grams per square centimetre. (b) $\theta_0^2(R)$ against R for water and Lucite.

A.1. The water-equivalent thickness

The water-equivalent ratio (WER) of a material is defined as the ratio of the stopping power of protons in the material over that in water. It depends only slightly on the proton energy.
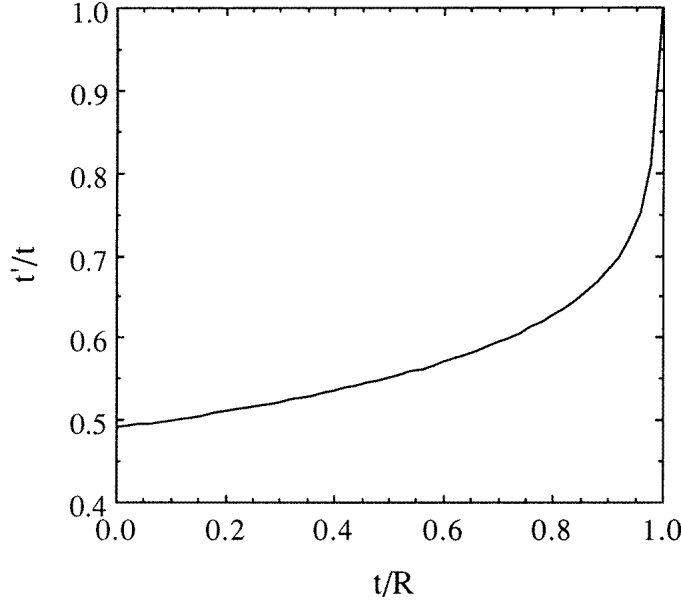
Figure A3. The scaling curve of t'/t against t/R for different materials and different initial proton energies. t is the areal thickness of the material in grams per square centimetre, t' is the effective thickness in grams per square centimetre and R is the mean proton range in grams per square centimetre.

As shown in figure A1, the WER of Lucite is almost a constant over a wide range of proton residual ranges, and it is a good approximation to take it as constant within the therapeutic range. For a degrader with a physical thickness l in centimetres the areal density in grams per square centimetre, t, is given by $t = l\rho$, where ρ is the density of the material in grams per cubic centimetre. The water-equivalent thickness of the degrader in grams per square centimetre, τ, is given by $\tau = t\,\text{WER}$. The WER values we used are 0.9762 for Lucite, 0.6597 for brass and 0.5006 for lead.

A.2. Scattering in intermediate-thickness materials

Consider a narrow mono-energetic proton beam passing through a degrader of finite thickness. The angular distribution is taken to be a Gaussian with the characteristic angle θ_0 given by the generalized Highland approximation.

$$\theta_0(t) = 14.1\left[1 + \frac{1}{9}\log_{10}\left(\frac{t}{L_R}\right)\right]\left[\int_{-\infty}^{t}\left(\frac{1}{pv}\right)^2\frac{\mathrm{d}t'}{L_R}\right]^{1/2} \tag{A1}$$

where t in grams per square centimetre is the areal density of the material, L_R in grams per square centimetre is the radiation length of the material, and pv in MeV is the product of momentum and the velocity of the protons at depth t' and varies, of course, with t'.
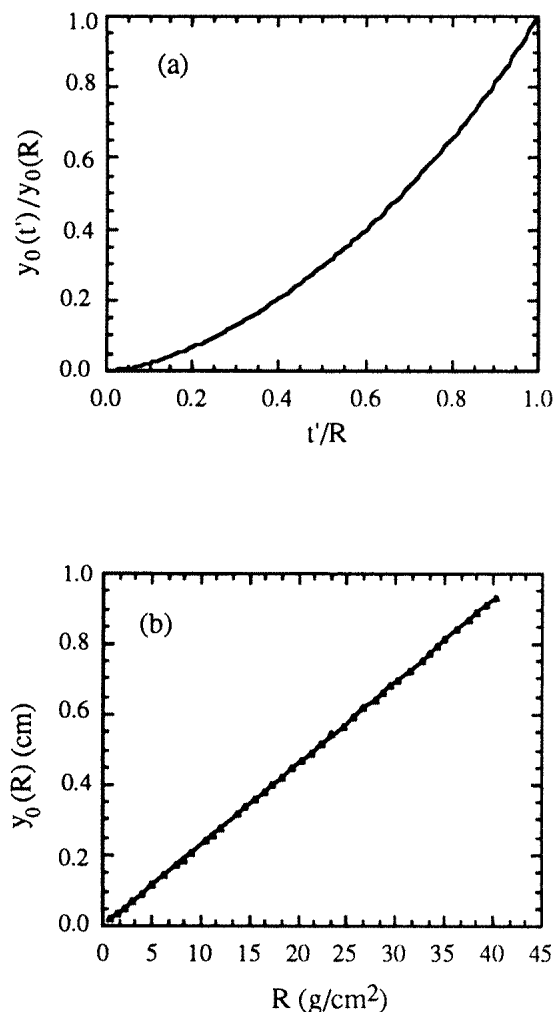
Figure A4. (a) The scaling curve of $y_0(t')/y_0(R)$ against t'/R for different materials and different input proton energies. (b) $y_0(R)$ against R for water. y_0 is in centimetres and R in grams per square centimetre. Data are fitted by the nearly straight line: $y_0(R) = 0.022\,75R + 0.120\,85 \times 10^{-4}R^2$.

For protons with mean range R, the ratio $(\theta_0(t)/\theta_0(R))^2$ as a function of t/R does not change much for a variety of materials and incident proton energies, as shown in figure A2(a). The variation of $\theta_0(R)$ with R, calculated for water and Lucite, is shown in figure A2(b).

The concept of effective origin of scattered particles in a thick target, as described by Gottschalk *et al* (1993), is used to correct the distance of the effective origin of scattering to the point of interest. The effective scattering origin of a degrader divided by the thickness of the degrader as a function of the thickness of the degrader normalized by the residual range of the protons is an essentially universal curve as shown in figure A3.

   In the implementation of our algorithm, we tabulate the results of figures A1–A3 (with water at 158.6 MeV incident energy) for quick look-up.

A.3. Scattering in infinitely thick materials (i.e. the patient)

For an infinitely narrow parallel mono-energetic beam entering an infinite medium—such as the patient—the radial distribution of fluence and dose at depth within the medium due to Coulomb scattering has a Gaussian distribution, with an rms radius at depth t', which can be calculated using the generalized Highland approximation as

$$y_0(t') = 14.1 \left(1 + \frac{1}{9} \log_{10} \left(\frac{t'}{L_R} \right) \right) \left[\int_0^{t'} \left(\frac{t'-z}{pv} \right)^2 \frac{\rho}{L_R} \, dz \right]^{1/2}. \tag{A2}$$

The rms scattering radius at depth t', divided by the rms scattering radius at the depth corresponding to the full residual range of the protons as they enter the medium, as a function of depth normalized by the full residual range, is a universal curve which is given in figure A4(a). The rms scattering radius in water at full residual range against full residual range is calculated and plotted in figure A4(b).

   In the implementation of our algorithm, we tabulate the results of figure A4 for quick look-up.

References

Barkas W H and Berger M J 1964 Studies of penetration of charged particles in matter *National Academy of Sciences–National Research Council, Washington, DC, Publication* 1133

Chen G T Y, Singh R P, Castro J R, Lyman J T and Quivey J M 1979 Treatment planning for heavy ion radio therapy *Int. J. Radiat. Oncol. Biol. Phys.* **5** 1809–19

Goitein M 1978 A technique for calculating the influence of thin inhomogeneities on charged particle beams *Med. Phys.* **5** 258–64

Gottschalk B, Koehler A M, Mayo C S and Wagner M S 1994 Proton beam technology: slit scattering and penumbra *Proton Therapy Co-Operative Group XX Meeting (Abstract) (Chester, 1994)*

Gottschalk B, Koehler A M, Schneider R J, Sisterson J M and Wagner M S 1993 Multiple Coulomb scattering of 160 MeV protons *Nucl. Instrum. Method* B **74** 467–90

Hogstrom K R, Mills M D and Almond P R 1981 Electron beam dose calculations *Phys. Med. Biol.* **26** 445–59

Janni J F 1966 Calculations of energy loss, range, pathlength, straggling, multiple scattering, and the probability of inelastic nuclear collisions for 0.1 to 1000 MeV protons *Air Force Weapons Laboratory Technical Report No. AFWL-TR-65-150*

Koehler A M, Schneider R J and Sisterson J M 1975 Range modulators for protons and heavy ions *Nucl. Instrum. Methods* **131** 437–40

Lee M, Nahum A E and Webb S 1993 An empirical method to build up a model of proton dose distribution for a radiotherapy treatment-planning package *Phys. Med. Biol.* **38** 989–98

Mayo C S, Gottschalk B and Wagner M 1993 Monte Carlo studies of edge scattering in proton beams *Proton Therapy Co-Operative Group XIX Meeting (Abstract) (Cambridge, MA, 1993)*

Petti P 1992 Differential-pencil-beam dose calculations for charged particles *Med. Phys.* **19** 137–49

Preston W M and Koehler A M 1968 The effects of scattering on small proton beams (Harvard University, unpublished)

Scheib S, Pedroni E, Blattmann H, Boehringer T, Coray A, Lin S, Munkel G and Schneider U 1992 3D-treatment planning and 3D-dose optimization for conformal proton therapy by voxel scanning *Proton Therapy Co-Operative Group XVII Meeting (Abstract) (Loma Linda, CA, 1992)*

Siddon R L 1985 Prism representation: a 3D ray-tracing algorithm for radiotherapy applications *Phys. Med. Biol.* **30** 817–24

Sisterson J M, Urie M, Koehler A M and Goitein M 1989 Distal penetration of proton beams: the effects of air gaps between compensating bolus and patient *Phys. Med. Biol.* **34** 1309–15

Urie M, Goitein M, Holley W R and Chen G T Y 1986a Degradation of the Bragg peak due to inhomogeneities *Phys. Med. Biol.* **31** 1–15

Urie M, Goitein M and Wagner M 1984 Compensating for heterogeneities in proton radiation *Phys. Med. Biol.* **29** 553–66

Urie M, Sisterson J M, Koehler A M, Goitein M and Zoesman J 1986b Proton beam penumbra: effects of separation between patient and beam modifying devices *Med. Phys.* **13** 734–41

Wagner M 1992 Ultimated measurement of treatment beams with a 48 diode array in a compact water phantom *Proton Therapy Co-Operative Group XVII Meeting (Loma Linda, CA, 1992)*

Wilson R R 1946 Radiological use of fast protons *Radiology* **47** 487–91